Nano-Micro Letters

ARTICLE

Hierarchical Polyimide Nonwoven Fabric with Ultralow-Reflectivity Electromagnetic Interference Shielding and High-Temperature Resistant Infrared Stealth Performance

Xinwei Tang[1], Yezi Lu[1], Shuangshuang Li[1], Mingyang Zhu[1], Zixuan Wang[1], Yan Li[2], Zaiyin Hu[3], Penglun Zheng[4], Zicheng Wang[1] ✉, Tianxi Liu[1] ✉

HIGHLIGHTS

- Hierarchical polyimide (PI) nonwoven fabric is fabricated by alkali treatment, in-situ growth of magnetic particles, and "self-activated" electroless Ag plating process.

- Impedance matching structure by assembling Fe_3O_4/Ag-loaded PI nonwoven fabric (PFA) and pure Ag-coated PI nonwoven fabric (PA) induces more electromagnetic waves enter PFA/PA and be dissipated.

- The fluffy 3D space structure of PFA with strong adhesion interaction and low infrared emissivity of PA endow PFA/PA with excellent thermal stability in electromagnetic interference shielding and high-temperature resistant infrared stealth performance.

ABSTRACT Designing and fabricating a compatible low-reflectivity electromagnetic interference (EMI) shielding/high-temperature resistant infrared stealth material possesses a critical significance in the field of military. Hence, a hierarchical polyimide (PI) nonwoven fabric is fabricated by alkali treatment, in-situ growth of magnetic particles and "self-activated" electroless Ag plating process. Especially, the hierarchical impedance matching can be constructed by systematically assembling Fe_3O_4/Ag-loaded PI nonwoven fabric (PFA) and pure Ag-coated PI nonwoven fabric (PA), endowing it with an ultralow-reflectivity EMI shielding performance. In addition, thermal insulation of fluffy three-dimensional (3D) space structure in PFA and low infrared emissivity of

PA originated from Ag plating bring an excellent infrared stealth performance. More importantly, the strong bonding interaction between Fe_3O_4, Ag, and PI fiber improves thermal stability in EMI shielding and high-temperature resistant infrared stealth performance. Such excellent comprehensive performance makes it promising for military tents to protect internal equipment from electromagnetic interference stemmed from adjacent equipment and/or enemy, and inhibit external infrared detection.

KEYWORDS Polyimide; Electromagnetic interference shielding; Low reflectivity; Infrared stealth; Compatibility

✉ Zicheng Wang, wangzc@jiangnan.edu.cn; Tianxi Liu, txliu@jiangnan.edu.cn

1 The Key Laboratory of Synthetic and Biological Colloids, Ministry of Education, School of Chemical and Material Engineering, International Joint Research Laboratory for Nano Energy Composites, Jiangnan University, Wuxi 214122, Jiangsu, People's Republic of China

2 Jiangsu Ferrotec Semiconductor Technology Co., Ltd., Yancheng 214000, Jiangsu, People's Republic of China

3 Guizhou Aerospace Wujiang Electro-Mechanical Equipment Co., Ltd., No. 20-5, Dalian Road Aerospace Industrial Park, Huichuan District, Zunyi City 563000, Guizhou, People's Republic of China

4 Civil Aircraft Fire Science and Safety Engineering Key Laboratory of Sichuan Province, College of Civil Aviation Safety Engineering, Civil Aviation Flight University of China, Guanghan 618307, Sichuan, People's Republic of China

1 Introduction

As the electronics and information industry rapidly develops, electromagnetic leakage and high-temperature infrared radiation become serious problems [1, 2]. Especially in the field of military protection, they easily lead to the information leakage and infrared exposure [3–6]. Hence, designing and fabricating compatible electromagnetic interference (EMI) shielding and infrared stealth material possesses a significant application value [2, 7, 8]. In comparison with those traditional metal and carbon-based nanomaterials, polymer-based composites attract increasing attention for EMI shielding and infrared stealth application, due to low density, corrosion resistance, low weight, and good processability [9–13].

Among them, metallized polymer nonwoven fabric gradually becomes a promising electromagnetic protection material, owning to its ultralight density, excellent flexibility, high electrical conductivity, and low infrared emissivity [14–17]. As reported [14], nickel-metallized polyimide nonwoven fabric is prepared by polydopamine roughening, palladium-free activation of chloroplatinic acid, electroless nickel plating, and octadecanethiol corrosion-resistant treatment. It exhibits a high electromagnetic interference shielding effectiveness (EMI SE) value of 68.6 dB, due to their high electrical conductivity (953 S cm^{-1}). However, its higher electrical conductivity usually leads to the generation of impedance mismatch on interface between material and air. Most of incident electromagnetic waves (EMWs) are reflected to the original medium. As a result, the reflected EMWs are prone to induce a secondary pollution, severely interfering the normal operation of adjacent electronic devices. Meanwhile, the introduction of metal coating endows the composite with an excellent thermal conductivity. The higher thermal conductivity transmits lots of heat energy derived from self-heating electrical equipment, thereby inducing the formation of obvious infrared radiation. The undesired infrared radiation is easily detected by infrared detectors. Therefore, how to realize the synergistic design and fabrication of compatible composites with low-reflectivity EMI shielding and infrared stealth performance gradually becomes a big challenge in the system of metallized polymer nonwoven fabric.

Many explorations have been attempted to assembly the efficient low-reflectivity electromagnetic interference (EMI)

shielding materials [18–22]. For example, Ma et al. successfully constructs multilayer CNF/MXene/FeCo composite film with controlled magnetic-conductivity dual-gradient structure by the layer-by-layer vacuum filtration method [19]. The composite film at a thickness of 340 μm exhibits an excellent EMI SE of 58.0 dB, whereas the corresponding R coefficient decreases to 0.61. However, a significant amount of EMW is still reflected due to its higher R coefficient, which needs to be further optimized. In addition, a high-performance infrared stealth material should be required to satisfy the Stefan–Boltzmann law: $E = \varepsilon \sigma T^4$, where E is the infrared radiation intensity of material, ε is the infrared (IR) emissivity, σ is the Stefan–Boltzmann constant, and T is the surface temperature [23–25]. Therefore, an excellent infrared stealth performance can be achieved by reducing the IR emissivity and/or surface temperature of material. To reduce the IR emissivity, the surface electrical conductivity of materials should be increased, enhancing the reflection of mid-far (3–5 and 8–14 μm) infrared radiations. For example, as reported by Deng et al. [26], a highly densified and large-area MXene coating is prepared by micro-crosslinking between catecholamine and MXene. As a consequence, MXene coating presents low IR emissivity (0.179) and infrared stealth performance. However, the ultrahigh electrical conductivity of 12,247 S cm^{-1} leads to the formation of impedance mismatch, causing serious secondary electromagnetic pollution. On the other hand, porous insulating materials are used to reduce surface temperatures by blocking the thermal diffusion originated from the high-temperature heat sources. As reported by Wang et al. [27], an ultralight and mechanically robust polyimide curly nanofibrous aerogels are prepared by manipulated the solution/water (H$_2$O) molecule interaction and ejection mode. As a result, those aerogels possess high porosity of 99.8% and excellent infrared stealth performance. However, the low permittivity and permeability of porous insulation materials are difficult to achieve effective dissipation of incident EMW, due to the existence of free space. To effectively dissipate the incident EMW, many functional nanofillers are introduced into porous materials. For example, Gu et al. successfully prepares a poly(3,4-ethylenedioxythiophene):poly(sodium styrenesulfonate)-coated melamine foam by dip-coating process [28]. As a result, the formation of porous structure in foam endows it with excellent infrared stealth ($\Delta T = 35.9$ °C) and microwave absorption properties ($RL_{min} = -57.57$ dB, d = 5 mm). However, the

thinker thickness significantly reduces the convenience of material. Moreover, the functional nanofiller for electromagnetic dissipation in porous insulation materials is generally introduced by in-situ compounding or vacuum impregnation methods. Nevertheless, the in-situ composite approach inevitably reduces the mechanical properties of composite. Additionally, although vacuum impregnation can be employed to build an electromagnetic dissipation network without altering mechanical properties, the weaker bonding force between the functional nanofiller and skeleton trough van der Waals interaction make it easy for the functional nanofiller to strip from skeleton, which seriously limits their durability in the high-temperature environments [29]. Therefore, it is difficult to achieve the integrated construction of electromagnetic interference shielding and high-temperature infrared stealth using only one material. How to realize the compatibility of low-reflectivity EMI shielding and high-temperature resistant infrared stealth becomes the huge challenge that needs to be solved urgently.

In this paper, a hierarchical polyimide (PI) nonwoven fabric with ultralow-reflectivity EMI shielding and high-temperature resistant infrared stealth performance are prepared by alkali treatment, in-situ growth of magnetic particles and "self-activated" electroless silver plating process. The alkali treatment facilitates the hydrolyzation of imide rings in PI molecules, thereby leaving abundant carboxylic active sites. Those carboxylic active sites can be served as strong bonding anchors for Ag nanoparticles generated by Ag^+ exchange and chemical reduction. It facilitates the effective "self-activated" deposition of Ag atoms during electroless silver plating process, leading to the formation of pure Ag-coated PI nonwoven fabric (PA). In addition, those carboxylic active sites provide strong adhesion for in-situ growth of magnetic particles (Fe_3O_4) through complexation with iron ions (Fe^{3+}) and annealing treatment. Subsequently, to further increase the quantity of active sites, dopamine (DA) can be polymerized on the surface of Fe_3O_4-loaded PI nonwoven fabric (PF) as a strong adhesion roughened coating. The catechol and amine functional groups remaining in polydopamine can further act as ligand/reduction agent for Ag^+. Those obtained Ag nanoparticles can accelerate the effective "self-activated" deposition of Ag atoms during electroless silver plating process. As a consequence, the impedance characteristic of Fe_3O_4/Ag-loaded PI nonwoven fabrics (PFA) can be easily adjusted by controlling the in-situ growth of magnetic particles and "self-activated" electroless silver plating process.

The synergistic fabrication of PFA and PA facilitates the rational construction of hierarchical impedance matching in PFA/PA. It induces more EMW enter the composite and be dissipated as much as possible, endowing it with an ultralow-reflectivity EMI shielding performance. Moreover, thermal insulation of fluffy 3D space structure in PFA and IR emissivity of PA originated from Ag plating bring a superior infrared stealth performance. More importantly, the strong adhesion interaction between Fe_3O_4, Ag, and PI fiber allows it resist the thermal stress derived from high-temperature source, enhancing the thermal stability in EMI shielding and high-temperature resistant infrared stealth performance. Such excellent compatible ultralow-reflectivity EMI shielding/infrared stealth performance makes it possible for PFA/PA to become a potential candidate with competitive advantage in military tent and/or camouflage.

2 Experimental Section

2.1 Materials

Tris(hydroxymethyl) aminomethane (Tris, $\geq 99\%$), dopamine (DA, $\geq 99\%$), dimethylaminoborane (DMAB, $\geq 97\%$), D-(+)-glucose ($\geq 99\%$), L-potassium sodium tartrate ($\geq 99\%$), and iron(III) chloride hexahydrate ($FeCl_3 \cdot 6H_2O$, $\geq 99\%$) were purchased from Adamas Reagent Co., Ltd. Ethanol ($\geq 99.7\%$), ammonium hydroxide aqueous solution ($NH_3 \cdot H_2O$, $25\% \sim 28\%$), silver nitrate ($AgNO_3$, $\geq 99.8\%$), and sodium hydroxide (NaOH, $\geq 96\%$) were purchased from Sinopharm Chemical Reagent Co., Ltd. 75 spray glue was purchased from Minnesota Mining and Machinery Company. All other chemicals were used without further purification as received.

2.2 Preparation of Ag-Coated Polyimide Nonwoven Fabrics

The hot-pressed and compact PI nonwoven fabric was prepared according to our previously reported method [30]. Subsequently, the compact PI nonwoven fabric was immersed in a 10 wt% NaOH solution for 3 min. Then, the obtained nonwoven fabric was sufficiently washed by deionized (DI) water. Afterward, the obtained nonwoven fabric was placed in 5 g L^{-1} $AgNO_3$ and 2 g L^{-1} DMAB solution

to be immersed for 2 and 0.5 h. Finally, the nonwoven fabric was fully washed with DI water and placed in an electroless Ag plating solution for x h (marked as PA_x). For electroless Ag plating solution, $AgNO_3$ was dissolved in deionized water, $NH_3 \cdot H_2O$ was added until the solution was clarified to obtain silver-ammonia solution. And then 50 mL of solution containing 80 g L^{-1} glucose, 2.5 g L^{-1} potassium sodium tartrate, and 100 g L^{-1} ethanol was added to the silver-ammonia solution.

2.3 Preparation of Fe₃O₄/Ag-Loaded Polyimide Nonwoven Fabrics

First, a fluffy PI nonwoven fabric was prepared according to our previously reported method [14, 31]. Subsequently, the nonwoven fabric was immersed in a 10 wt% NaOH solution for 3 min. Afterward, the obtained nonwoven fabric was washed sufficiently by DI water to remove residual NaOH. Then, the obtained nonwoven fabric was placed in a 37 wt% solution of $FeCl_3 \cdot 6H_2O$ at 80 °C for 5 h. Afterward, the treated PI nonwoven fabric was washed by anhydrous ethanol and then placed in an oven at 80 °C for 2 h. Finally, the dried PI nonwoven fabric was treated in a tube furnace and heated up to 400 °C at a rate of 5 °C min^{-1} in an atmosphere of 12 vol% hydrogen-argon (H_2/Ar) mixture. Afterward, the nonwoven fabric was treated at 400 °C for 4 h. As a results, magnetic nanoparticle-coated PI fiber (PF) was obtained. PF nonwoven fabric was then placed in 10 mM Tris solution at pH = 8.5. 2 g L^{-1} DA was added, and the reaction was carried out under magnetic stirring for 24 h. After the reaction, the obtained nonwoven fabric was washed sufficiently with DI water. And then it was placed in 5 g L^{-1} $AgNO_3$ to be immersed for 2 h. Afterward, the nonwoven fabric was fully washed with DI water and placed in a electroless Ag plating solution for y h (marked as PFA_y). Therefore, PF can be also labeled as PFA_0.

2.4 Preparation of Hierarchical Polyimide Composite Nonwoven Fabrics

The hierarchical polyimide nonwoven fabric was prepared by combining PA_x with different thicknesses of PFA_y. Finally, the nonwoven fabric was pasted by 75 spray glue, which was denoted as PFA_y/PA_x (or PFA/PA if not emphasized).

2.5 Characterizations

The morphology of the specimens was observed by a field emission scanning electron microscope (FE-SEM) at an accelerating voltage of 30 kV. Energy-dispersive X-ray spectroscopy (EDS) analysis was also performed to analyze the surface composition of materials. X-ray diffraction (XRD) pattern was characterized on a Bruker D2 X-ray diffractometer with a Cu Kα X-ray source ($\lambda = 1.5418$ Å). X-ray photoelectron spectroscopic (XPS) was conducted on an ESCA 2000 (VG Micro-Tech, UK) using a monochromic Al Kα X-ray source. Thermal gravimetric analysis (TGA) was carried out using a TGA/DSC1/1100SF system under a N_2 atmosphere at a heating rate of 10 °C min^{-1}. Polyimide nonwoven fabric was prepared by electrostatic spinning machine (ET-2535H, Beijing Ucalery Co., Ltd., China). The sheet resistance (R) of nonwoven fabric was measured by the four-probe method with a ST2263 double electric measuring digital four-probe tester at room temperature. The electrical conductivity (σ) was obtained by the Eq. 1 [32]:

$$\sigma = \frac{1}{S} \cdot \frac{1}{R/L} = \frac{L}{R \cdot w \cdot t} \tag{1}$$

where σ was the electrical conductivity (S cm^{-1}), R was the sheet resistance (Ω sq^{-1}), L and S were the length (cm) and cross-sectional area (cm^2) of sample, and w and t were the width (cm) and thickness (cm). Using Agilent E5234B vector network analyzer and waveguide method, EMI SE was measured in X-band (8.2–12.4 GHz), Ku-band (12.4–18 GHz), K-band (18–26.5 GHz), and Ka-band (26.5–40 GHz). The corresponding EMI SE (SE or SE_T) can be obtained by calculating the scattering parameters (S_{11} and S_{21}) as follow Eqs. 2–7 [33, 34]:

$$R = |S_{11}|^2 = |S_{22}|^2 \tag{2}$$

$$T = |S_{21}|^2 = |S_{12}|^2 \tag{3}$$

$$A = 1 - R - T \tag{4}$$

$$SE_R = -10 \log (1 - R) = -10 \log \left(1 - |S_{11}|^2 \right) \tag{5}$$

$$SE_A = -10 \log \left(\frac{T}{1-R} \right) = -10 \log \left(\frac{|S_{21}|^2}{1 - |S_{11}|^2} \right) \tag{6}$$

$$SE_T = SE_R + SE_A + SE_M \tag{7}$$

when the SE_T exceeded 10 dB, SE_M can be generally negligible. Reflectivity values (dB) were calculated by the measured S_{11} according to the Eq. 8, which denoted the microwave absorption performance of the nonwoven fabrics for incident EMW [35, 36].

$$Reflectivity = 10 \log R = 10 \log |S_{11}|^2 \tag{8}$$

Furthermore, a self-made electromagnetic wave transmitter–receiver (10.5 GHz, 1W) and a wireless projector (PeakDo, 60 GHz, Shenzhen Xiwei Digital Technology Co., Ltd.) were carried out to demonstrate the EMI shielding performance of samples. Paperless recorder with thermocouple (MIK-R2007, Hangzhou Miko sensor Co., Ltd.) was applied to record the changes in the surface temperature of samples. The nonwoven fabric was placed on a thermal stage (100 mm*100 mm, Shenzhen Jinglianghe Technology Co., Ltd.) to evaluate the infrared stealth performance (FLUKE Ti400＋, Fluke Corporation of the USA). The IR emissivity (ε) was calculated by Eq. 9 after testing the reflectivity (r) and transmissivity (t) [37].

$$\varepsilon = 1 - r - t \tag{9}$$

The t and r were obtained from Fourier transform infrared spectroscopy (FTIR, Nicolet IS50, Thermo Fisher Scientific Inc., USA) with an integrating sphere.

3 Results and Discussion

3.1 Structure and Morphology of Composite Nonwoven Fabrics

The fabrication process of hierarchical polyimide (PFA/PA) nonwoven fabrics is demonstrated in Scheme 1. Firstly, PI nonwoven fabrics are prepared by a reported previous method [14, 31]. As we know, polyimide possesses high surface inertness [38–40]. Hence, the weaker bonding force between the functional nanofiller and PI fiber makes it easy for the functional nanofiller to exfoliate from polyimide fiber. To increase the surface activity of PI fiber, alkali etching treatment is applied by NaOH solution to promote the hydrolyzation of imide ring on the surface of PI fiber, thereby leaving abundant carboxyl active sites [41, 42]. As shown in Fig. S1a, c, the original PI fiber displays a smooth surface. After NaOH treatment, the obtained fiber presents a distinctly rough surface as displayed in Fig. S1b, d. It confirms the effectiveness of alkali etching. Based on the above, those carboxylic active sites can be act as strong bonding "chemical" anchors for Ag nanoparticles generated by Ag⁺ exchange and chemical reduction. As shown in Fig. S2, Ag nanoparticles with a diameter of ~ 30 nm can be effectively reduced by DMAB and uniformly deposited to the surface of PI fiber. More importantly, those Ag nanoparticles can be further acted as the "self-activated" center to accelerate the deposition rate of Ag atom during the electroless Ag plating process [43]. As shown in Fig. 1a–d, a compact plating can be successfully formed on the surface of PI fiber. Meanwhile, the plating degree of Ag can be further optimized as the electroless plating time increases. Specifically, the obtained Ag could not even cover the surface of PI fibers, as the plating time is less than 1 h (Fig. 1b). Some blanks/defects leave on PA_1. Those blanks/defects can be effectively compensated when the plating time is prolonged to 1.5 h. The corresponding surface of $PA_{1.5}$ becomes smoother (Fig. 1c). When the plating times are further prolonged to 2 h, the surface of PA_2 becomes rough, which may be attributed to the excess Ag plating (Fig. 1d). It is inevitable that the undesired aggregation of Ag nanoparticles would lead to increase in roughness of fiber. Meanwhile, it can be distinctly observed that the color of nonwoven fabric transfers from bright yellow of PI to silver-white (Fig. 2h) after electroless Ag plating. It indirectly indicates the effectiveness of Ag deposition. To further demonstrate the successful preparation of modified polyimide composites, the nonwoven fabric is also characterized by X-ray diffraction spectra (XRD). As displayed in Fig. 2a, a visible characteristic diffraction peak located at 38° arise in curve of $PA_{1.5}$ in compared with that of PI. It can be assigned to the plane (111) of face-centered cubic phase of Ag. In order to further probe the surface chemical change, those nonwoven fabrics are characterized by X-ray photoelectron spectroscopy (XPS). As show in Fig. 2d, a new peak of Ag elements located at 368.8 eV appears in $PA_{1.5}$. Based on the above, it can be concluded that Ag is successfully loaded on the surface of PI fiber by "self-activated" electroless Ag plating. In addition, the electrical conductivity of PA_x is measured and recorded. As shown in Fig. 2c, it presents a progressive tendency to increase from 385 (1 h) to 531.4 S cm⁻¹ (1.5 h), and then to 656.2 S cm⁻¹ (2 h) with the increasing the electroless Ag plating time. Therefore, the adjustable impedance characteristic of PA_x can be endowed
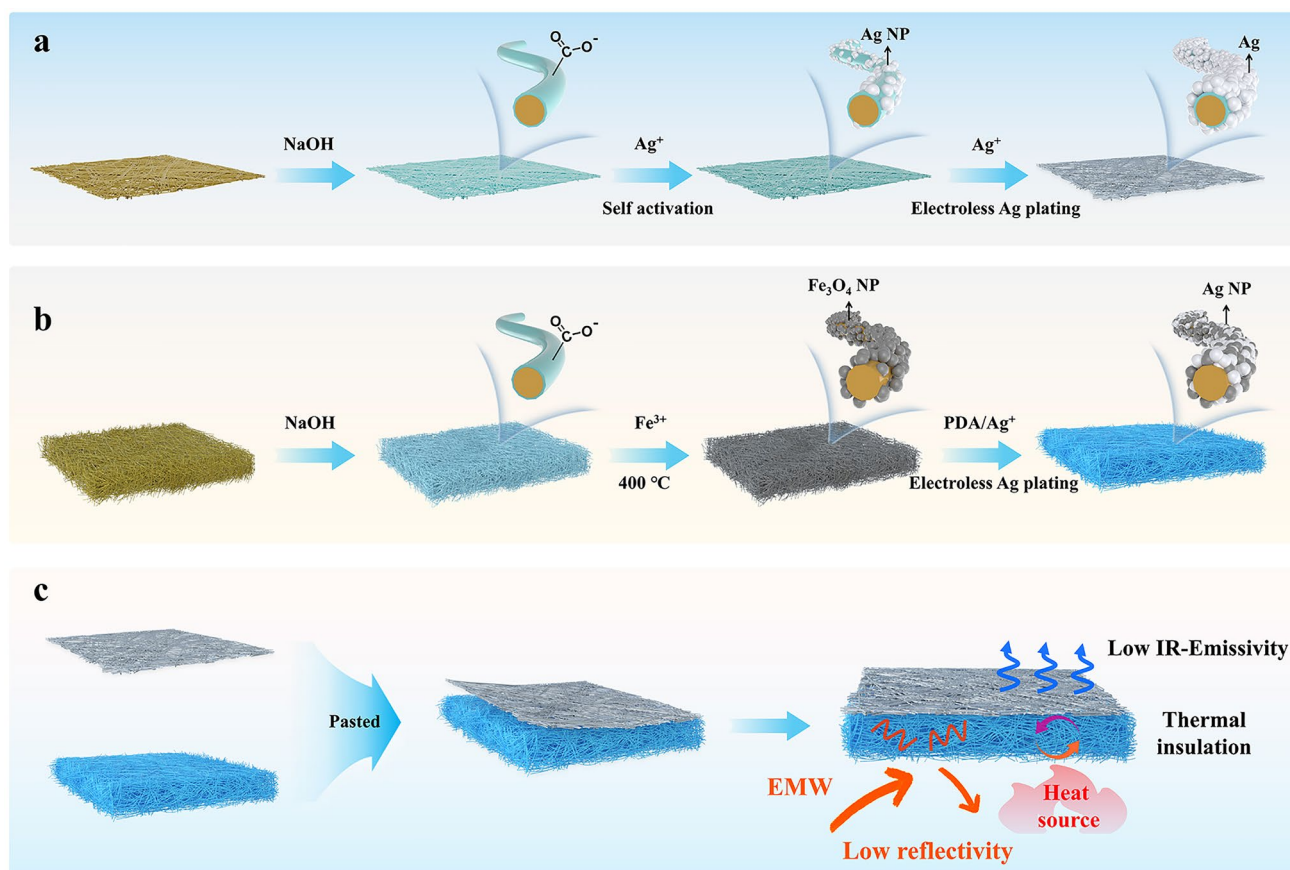
Scheme 1 Schematic illustration of the preparation process of PFA/PA nonwoven fabrics

by the different electrical conductivities. Moreover, the corresponding density exhibits a similar tendency increase from 0.45 to 0.55 g cm^{-3} (Fig. 2c), which demonstrates the PA$_x$ nonwoven fabric possesses a light characteristic.

Moreover, those carboxylic active sites can provide strong adhesion for in-situ growth of magnetic particles (Fe$_3$O$_4$) through complexation with iron ions (Fe^{3+}) and annealing treatment. Specifically, the high temperature (400 °C) and H$_2$ can act as a reducing agent for Fe^{3+} during annealing treatment in H$_2$/Ar atmosphere. During annealing treatment, a part of Fe^{3+} can be reduced to Fe^{2+}. As a result, Fe$_3$O$_4$ nanoparticle can be prepared by annealing treatment in H$_2$/Ar atmosphere [44]. As demonstrated in Fig. 1e, f, Fe$_3$O$_4$ nanoparticles are successfully loaded on the surface of PI fiber. The corresponding energy-dispersive spectrometer (EDS) results demonstrate that Fe element is successfully distributed on the surface of PI fiber (Fig. S3). Similarly, XRD is utilized to analyze the crystalline structure of magnetic PI-based nonwoven fabric (PFA$_0$). In comparison with PI, a series of new diffraction

peaks for PFA$_0$ appears at 30°, 35°, 43°, 53°, 56°, and 62° as described in Fig. 2a. Those diffraction peaks correspond to the indexed planes of Fe$_3$O$_4$ (JCPDS No. 19-0629), which is indirectly confirm the formation of Fe$_3$O$_4$ on the surface of PI fiber. Furthermore, the high-resolution XPS spectra of Fe 2p for PFA$_0$ can be differentiated into four characteristic peaks to Fe 2$p_{3/2}$ and Fe 2$p_{1/2}$ at 710.8, 713.9, 724.2, and 727.3 eV, respectively (Fig. 2e). Meanwhile, those two satellite peaks of Fe 2$p_{3/2}$ and Fe 2$p_{1/2}$ appear at 719.1 and 733.1 eV. It indicates that the valence state of Fe in PFA$_0$ is Fe^{3+} and Fe^{2+} [45]. High resolution XPS spectra of O 1s of PFA$_0$ are also given in Fig. S4. Two peaks located at 530.0 and 531.5 eV respond to Fe–O and C=O. Those results once again confirm the formation of Fe$_3$O$_4$ on the surface of PI fiber. However, the exposed area of PI fibers is reduced, due to the loading of Fe$_3$O$_4$ nanoparticles covered on the surface of PI fibers. PFA$_0$ fiber possesses less sites to be treated by NaOH, thereby further hindering the achievement of subsequent "self-activated" electroless Ag plating. As a result, it is difficult to realize the effective
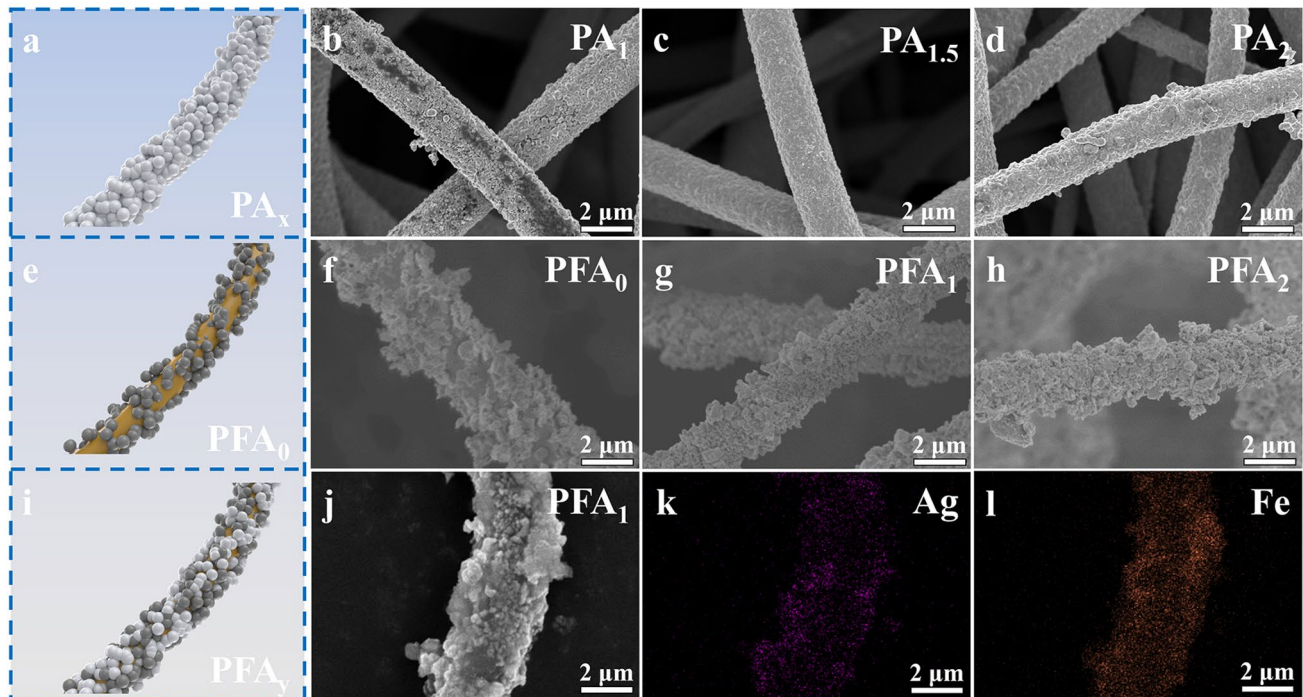
Fig. 1 Schematic illustration of **a** PA_x, **e** PFA_0, and **i** PFA_y. SEM images of **b** PA_1, **c** $PA_{1.5}$, **d** PA_2, **f** PFA_0, **g** and **j** PFA_1, **h** PFA_2 fiber, and **k, l** EDS mapping images of PFA_1 fiber

adjustability in impedance characteristic of PFA. Hence, dopamine (DA) with abundant catechol and amine functional groups is employed to increase the quantity of active sites as a roughening agent, which can be polymerized on the surface of PFA_0 fiber. The abundant hydroxyl groups on the surface of PDA will give PFA_0 fibers excellent hydrophilicity [37]. As shown in Fig. S5, the water contact angle transforms from 125.8° (PFA_0) to 29.6° (PFA_0/PDA). It indirectly indicates that PDA is successfully polymerized on the surface of PFA_0 fibers. Very importantly, the obtained PDA coating also possesses a strong adhesion, due to the residual catechol and amine functional groups in PDA. It provides a strong bonding force at the interfaces between subsequent Ag nanoparticles and PFA_0 fibers [46, 47]. Additionally, the residual catechol and amine functional groups in PDA molecules endow PDA with an excellent adsorption and reduction capabilities for Ag^+ [48]. As a result, PDA coating can also act as ligand/reduction agent to facilitate the in-situ immobilization/reduction of Ag^+ to Ag nanoparticle. Those Ag nanoparticles can serve as a "self-activated" center to accelerate the reduction reaction of Ag atom during electroless silver plating. As shown in Fig. 1f, the obtained Fe_3O_4 nanoparticle even can't cover

the whole surface of PI fiber, when the electroless Ag plating is not applied. Some gaps/defects leave on the surface of PI fiber. As the electroless Ag plating time is increased to 1 h, the surface of PFA_1 becomes rougher (Fig. 1g). As shown in a higher magnification SEM image of PFA_1 (Fig. S6), Ag nanoparticles show a smaller diameter compared to that of Fe_3O_4 particles. Ag nanoparticles effectively compensate those gaps/defects left from Fe_3O_4, and cover the original Fe_3O_4. When the electroless Ag plating time is prolonged to 2 h, more Ag nanoparticles are deposited, leading to an increase in the roughness of PFA_2 (Fig. 1h). Moreover, for PFA_1, the plane (111) of face-centered cubic phase of Ag appears at 38° as compared to PFA_0 (Fig. 2a). It indicates that Ag is successfully deposited on the surface of PFA_1 by electroless Ag plating. EDS is also employed to characterize the elements changes in PFA_x fiber before and after electroless Ag plating. As shown in Figs. 1j–l and S7, Ag element displays a uniform and distinct distribution on the surface of PFA_1 fiber, compared to the PFA_0 (Fig. S3). It once again confirms that Ag is successfully loaded on the surface of PFA_1 fiber. In addition, to further probe the surface chemical change, those nonwoven fabrics are characterized by XPS. As shown in Fig. 2d, Fe elements exist
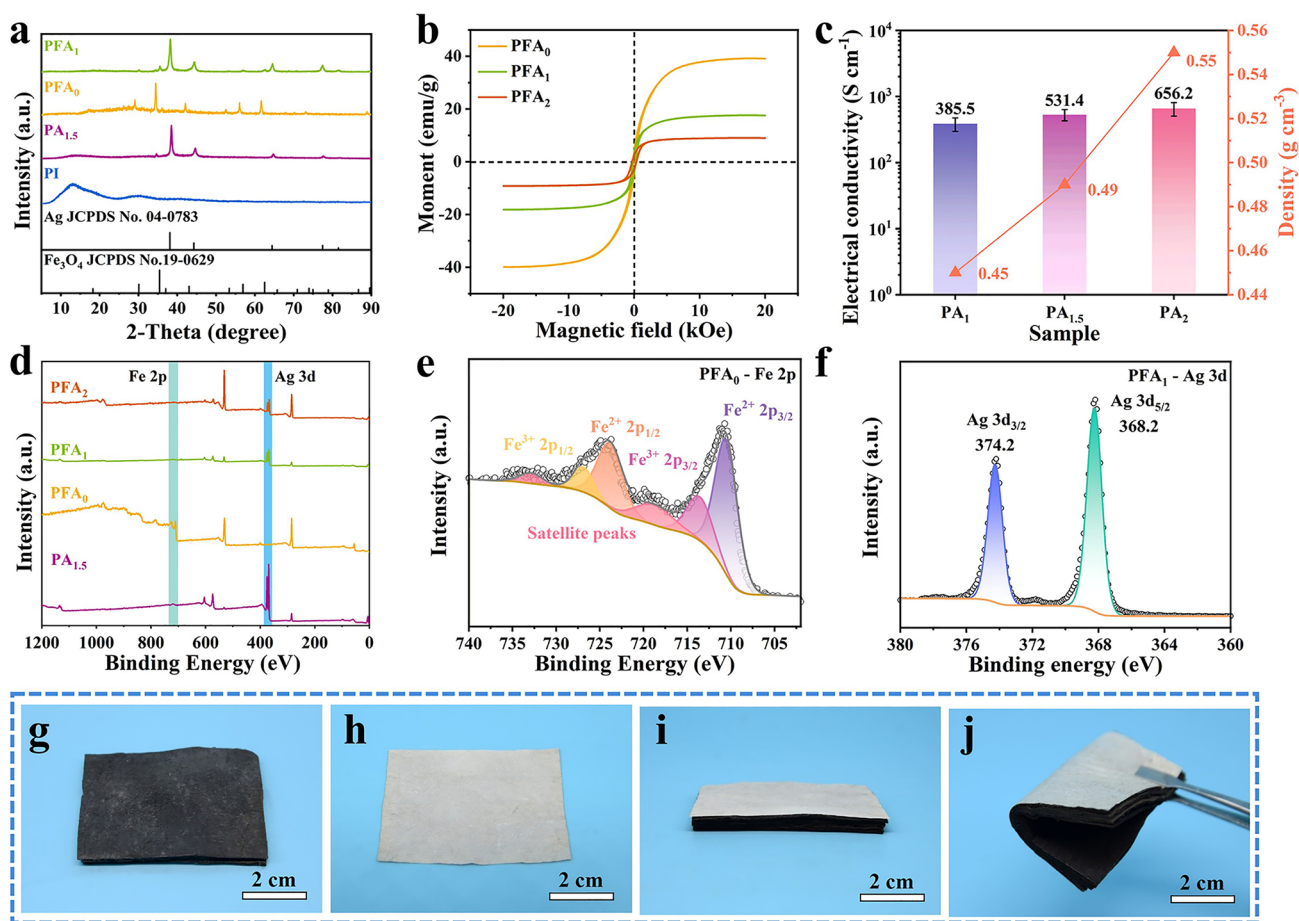
Fig. 2 **a** XRD patterns of PI, $PA_{1.5}$, PFA_0, and PFA_1. **b** Hysteresis loops of PFA_0, PFA_1, and PFA_2. **c** Electrical conductivity and density of PA_1, $PA_{1.5}$, and PA_2. **d** XPS spectra of $PA_{1.5}$, PFA_0, PFA_1, and PFA_2. High resolution XPS spectra of Fe $2p$ for **e** PFA_0 and **f** Ag $3d$ for PFA_1. Optical photograph of **g** 4*PFA_1, **h** $PA_{1.5}$, and **i**, **j** 4*PFA_1/$PA_{1.5}$

in PFA_0, PFA_1, and PFA_2. Compared with PFA_0, the characteristic peak of Fe $2p$ significantly reduces in XPS curves of PFA_1 and PFA_2. It may be ascribed to the fact that Fe_3O_4 is gradually covered by Ag with the increasing content of electroless Ag plating. Meanwhile, vibrating-sample magnetometer (VSM) is employed to characterize the evolution in magnetic properties of PFA_y under different electroless Ag plating times. Compared with PFA_0, the saturation magnetization (Ms) gradually decreases with increasing plating time as shown in Fig. 2b. In detail, PFA_0 exhibits a high Ms value of 39.20 emu g^{-1}, while that of PFA_1 and PFA_2 decreases to 17.64 to 9.05 emu g^{-1}, respectively. It can be also ascribed to the increasing content of electroless Ag plating, resulting in a corresponding decrease in the proportion of Fe_3O_4 in PFA_y. More importantly, the nonwoven fabrics do not undergo significant thermal decomposition

until 400 °C (Fig. S8). It indicates that those nonwoven fabrics possess excellent thermal stability after in-situ growth of magnetic particles and "self-activated" electroless Ag plating process. In addition, the residual yield of $PA_{1.5}$, PFA_0, and PFA_1 nonwoven fabrics is significantly higher than that of pure PI at higher temperature of 1000 °C, which once again confirms the excellent thermal stability of PFA. It can be attributed to the passivation of Fe_3O_4 and Ag plating formed on the surface of PI fibers. Besides, as shown in Fig. 2f, the Ag $3d$ region of PFA_1 can be further divided into Ag $3d_{5/2}$ (368.2 eV) and Ag $3d_{3/2}$ (374.2 eV). Both of them can be recognized as Ag^0 species [49]. Such results once again indicate that Ag is successfully obtained on PFA_0 by electroless Ag plating. As a consequence, the final PFA_y nonwoven fabric presents a uniform black in color (Fig. 2g).

As a conclusion, the impedance characteristic of nonwoven fabrics can be easily adjusted by controlling the in-situ growth of magnetic particles and "self-activated" electroless Ag plating process. The synergistic fabrication of Fe_3O_4/Ag-loaded PI nonwoven fabric (PFA_y) and pure Ag-coated PI nonwoven fabric (PA_x) facilitates the construction of hierarchical impedance matching in PFA_y/PA_x. As shown in Fig. 2i, four layers of PFA_1 with a thickness of 2.4 mm ($4*PFA_1$) and a layer of $PA_{1.5}$ with a thickness of 0.06 mm can be easily bonded by spray glue. The obtained $4*PFA_1$/$PA_{1.5}$ exhibits color difference in positive and negative surfaces. Importantly, $4*PFA_1$/$PA_{1.5}$ possesses an excellent flexibility. It can be bent at a wide angles (Fig. 2j), which is adapt to complex environments as an excellent flexible material.

3.2 Ultralow-Reflectivity EMI Shielding Performance of Nonwoven Fabrics

As we all known, the construction of electromagnetic matching facilitates the introduction of EMW enter the interior of nonwoven fabric and be dissipated as much as possible, thereby endowing it with an excellent low-reflectivity EMI shielding performance. To clarify the role of PFA_y in the electromagnetic matching structure, PFA_1 with different thicknesses ($N*PFA_1$) is obtained by the same approach to further investigate their EMI shielding performance. The electromagnetic S parameters of those samples are measured in the frequency range of 8.2–12.4 GHz. Based on the electromagnetic S parameters, the final SE_T, SE_A, and SE_R can be calculated according to Eqs. 2–7. As displayed in Fig. S9a, SE_T of PFA_1 exhibits an obvious tendency to increase form 2.1 dB (0.6 mm) to 3.9 dB (1.2 mm), 4.9 dB (1.8 mm), and then to 6 dB (2.4 mm) with the increasing thickness. However, they are much lower than that of commercial requirement (> 20 dB). In order to further clarify the EMI shielding mechanism, power coefficients of those samples can be calculated by Eqs. 2–4. As shown in Fig. S9b–d, the corresponding A and R coefficients exhibit a similar tendency to increase as the thickness of PFA_1 increases, whereas T coefficient displays an opposite case. Especially, T coefficient of $1*PFA_1$ with a thickness of 0.6 mm is up to a high value (> 0.5) in X-band. It suggests that most of incident EMW penetrates the thin sample. When the thickness of PFA_1 increases, the corresponding T coefficient decreases. It may be attributed to a fact that the increasing thickness of

PFA_1 effectively promotes the prolongation of EMW dissipation route, thereby endowing it with an increasing A coefficient and a decreasing T coefficient. Even so, the final T coefficient of $4*PFA_1$ is still maintained at a value of ~ 0.2. To further reduce the T coefficient, a high-reflectivity EMI shielding material should be introduced into the system.

Therefore, $PA_{1.5}$ (0.06 mm) with a high electrical conductivity (531.4 S cm^{-1}) is adhered on the backside of $N*PFA_1$. As a control, the pure $0*PFA_1$/$PA_{1.5}$ nonwoven fabric ($PA_{1.5}$) possesses a high EMI SE value of 67.5 dB in X-band. Based on the above, EMI SE performance of $N*PFA_1$/$PA_{1.5}$ can be further enhanced to a higher value (> 67.5 dB) as displayed in Fig. 3a, b. It once again confirms the effectiveness of $PA_{1.5}$ as high-reflectivity EMI shielding material. Meanwhile, EMI SE curve of $N*PFA_1$/$PA_{1.5}$ exhibits a tendency to increase from 71 to 77 dB with the increasing thickness of PFA_1. It agrees well with the above result in Fig. S9. To further investigate the difference of EMI shielding mechanism, SE_A, SE_R, and power coefficients are also calculated and demonstrated in Fig. 3b, e. It is worthy to note that SE_R of $N*PFA_1$/$PA_{1.5}$ decreases from 16 to 0.4 dB with the increasing thickness of PFA_1. Meanwhile, the corresponding A and R coefficient of $N*PFA_1$/$PA_{1.5}$ exhibit an opposite tendency. In detail, A coefficient increases from 0.03 to 0.35, to 0.51, to 0.65, and then to 0.91 with the increasing the thickness of PFA_1 from 0 to 2.4 mm (Fig. 3c, e). The corresponding R coefficient decreases from 0.97 to 0.65, to 0.49, to 0.35, and then to 0.09. It may be attributed to a fact that the increasing thickness of PFA_1 effectively prolongs the dissipation route of incident EMW. To further evaluate the dissipation capacity of $N*PFA_1$/$PA_{1.5}$ for EMW, reflectivity (dB) is calculated by Eq. 8. As displayed in Fig. 3f, reflectivity of $N*PFA_1$/$PA_{1.5}$ in X-band presents a tendency to decrease as the thickness of PFA_1 increases. In detail, $0*PFA_1$/$PA_{1.5}$ exhibits a high reflectivity (~ 0 dB). It suggests that almost EMW are reflected on the surface of $0*PFA_1$/$PA_{1.5}$. The corresponding reflectivity of $N*PFA_1$/$PA_{1.5}$ decreases from ~ − 2 to ~ − 12 dB, as the thickness of PFA_1 increases from 0.6 to 2.4 mm. It may be also explained by the increasing thickness of PFA_1. It can effectively lengthen the dissipation route of EMW, resulting in an increasing absorption and a decreasing reflection for EMW. More importantly, reflectivity of $4*PFA_1$/$PA_{1.5}$ is lower than -10 dB in 10.3–12.4 GHz. It indicates that more than 90% of incident EMW can be absorbed in $4*PFA_1$/$PA_{1.5}$. Therefore, $4*PFA_1$/$PA_{1.5}$ exhibits a huge
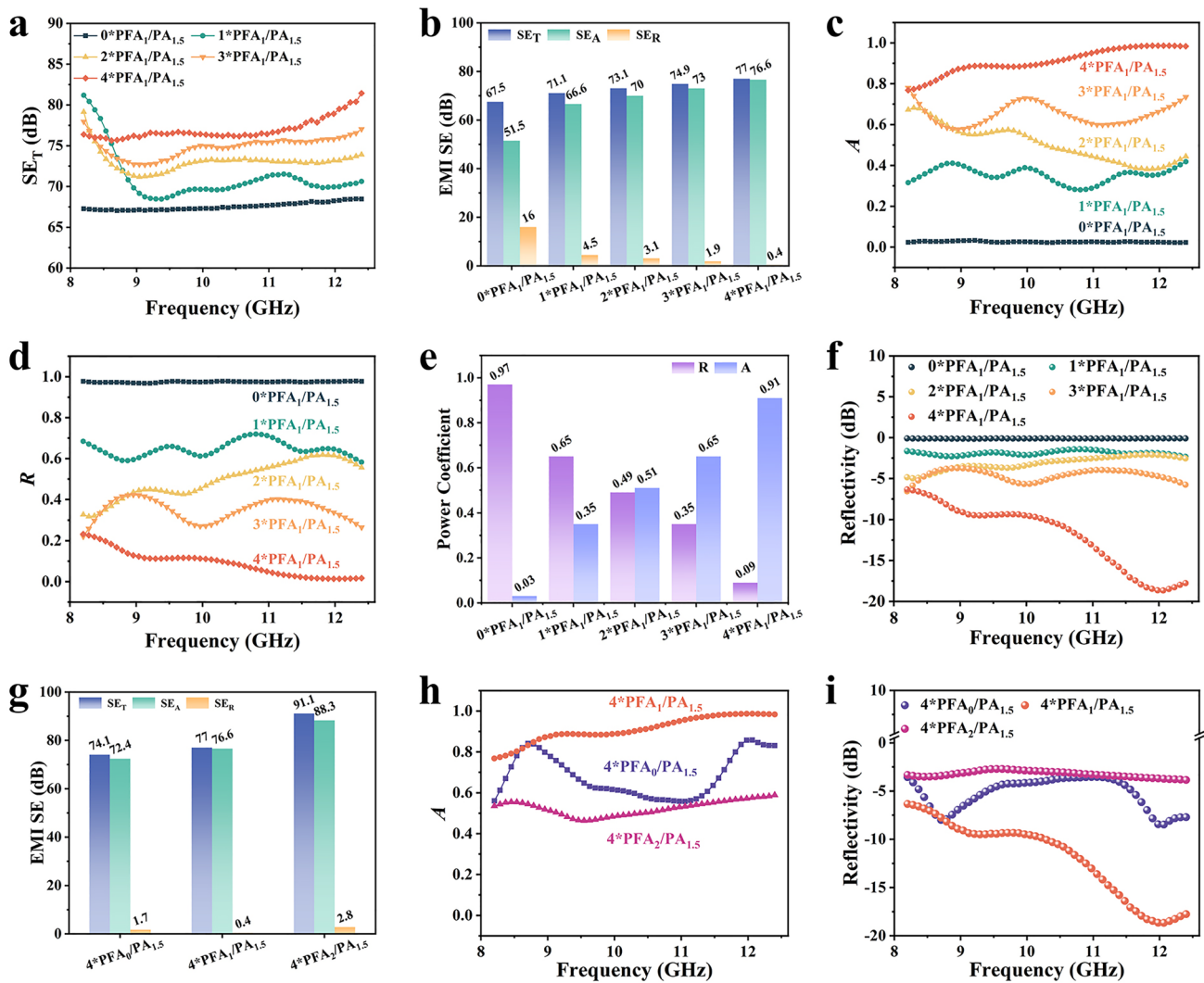
Fig. 3 **a** SE_T, **b** EMI SE, **c** A, **d** R, **e** power coefficient, **f** reflectivity patterns of $N*PFA_1/PA_{1.5}$, **g** EMI SE, **h** A, and **i** reflectivity patterns of $4*PFA_x/PA_{1.5}$

promise to be employed as a superior radar stealth material in 10.3–12.4 GHz.

As we all known, the impedance characteristic of samples are the key factors for fabricating low-reflectivity EMI shielding materials. Those EMI SE and power coefficients of PFA_x with different electroless Ag plating times are presented in Fig. S10. Without Ag plating, $4*PFA_0$ exhibits an ultralow EMI SE_T value of 1.9 dB in X-band. When the electroless Ag plating time is prolonged to 1 and 2 h, the corresponding SE_T of $4*PFA_x$ increases to 6 and 23 dB (Fig. S10a), respectively. Meanwhile, T coefficient of $4*PFA_x$ displays an outstanding tendency to decrease from ~0.65 ($4*PFA_0$) to ~0.25 ($4*PFA_1$), and then to ~0 ($4*PFA_2$), as

shown in Fig. S10d. It can be attributed to the increase in conductive Ag nanoparticle content, resulting in the increase in absorption and reflection capacity of PFA_x. In detail, R coefficient exhibits a prominent increase from ~0.01 ($4*PFA_0$) to ~0.2 ($4*PFA_1$), and then to 0.44 ($4*PFA_2$), as displayed in Fig. S10c. As a result, the corresponding A coefficient varies from ~0.3 ($4*PFA_0$) to ~0.53 ($4*PFA_1$) and maintains at ~0.55 ($4*PFA_2$), as shown in Fig. S10b. Those dynamic evolutions may be ascribed to the changing impedance characteristic of $4*PFA_x$. As to $4*PFA_2$, longer electroless Ag plating time endows it with higher electrical conductivity, thereby bringing an excellent EMI shielding performance (> 20 dB) with a low T coefficient and a high A

and R coefficients. Such results indirectly confirm the effectiveness of electroless Ag plating time on modulating the impedance characteristic of 4*PFA$_x$.

As a consequence, 4*PFA$_x$ can be further assembled with PA$_{1.5}$ to investigate the effect of construction of impedance matching structure on EMI shielding performance of sample. As shown in Fig. 3g, EMI SE$_T$ of 4*PFA$_x$/PA$_{1.5}$ shows a gradual tendency to increase from 74.1 dB (4*PFA$_0$/PA$_{1.5}$) to 77 dB (4*PFA$_1$/PA$_{1.5}$), and then to 91.1 dB (4*PFA$_2$/PA$_{1.5}$), due to the improved EMI SE performance of 4*PFA$_x$ (Fig. S10). More importantly, PFA$_x$/PA$_{1.5}$ exhibits ultralow SE$_R$ (< 3 dB) in X-band. As displayed in Fig. 3g, 4*PFA$_1$/PA$_{1.5}$ possesses the lowest SE$_R$ of 0.4 dB, compared to that of 4*PFA$_0$/PA$_{1.5}$ (1.7 dB) and 4*PFA$_2$/PA$_{1.5}$ (2.8 dB). To analyze the mechanism of EMI shielding performance for 4*PFA$_x$/PA$_{1.5}$, the corresponding A and R coefficients are also calculated and shown in Figs. 3h and S11. It can be obviously seen that R coefficient exhibits a tendency to firstly decreases, and then to increase with the increasing Ag content in PFA$_x$. Such results confirm the effectiveness of impedance matching structure on low-reflectivity EMI

shielding performance. For 4*PFA$_0$/PA$_{1.5}$, 4*PFA$_0$ possesses a high T coefficient due to the low Ag nanoparticle content (Fig. S10d). Hence, EMW can easily penetrate 4*PFA$_0$, and sharply be reflected at the surface of PA$_{1.5}$. Furthermore, EMW is rarely dissipated within 4*PFA$_0$, resulting in a high R and low A coefficient for 4*PFA$_0$/PA$_{1.5}$. As to 4*PFA$_2$/PA$_{1.5}$, the higher Ag nanoparticle content endows 4*PFA$_2$ with a high R coefficient as shown in Fig. S10c. In this case, most of EMW will be reflected at the surface of 4*PFA$_2$, due to the formation of impedance mismatch between air and 4*PFA$_2$. Only a few of EMW can enter 4*PFA$_2$ to be attenuated. Therefore, a high R coefficient of ~ 0.4 can be obtained for 4*PFA$_2$/PA$_{1.5}$. In contrast, 4*PFA$_1$ with moderate R coefficient (~ 0.2) can effectively induce most of EMW enter 4*PFA$_1$ and be dissipated as much as possible, owning to the formation of rational impedance matching between air, 4*PFA$_1$, and PA$_{1.5}$. Meanwhile, similar tendency arises in the Reflectivity of 4*PFA$_x$/PA$_{1.5}$ (Fig. 3i). 4*PFA$_1$/PA$_{1.5}$ exhibits the lowest reflectivity, which indicates that the least EMW reflection arises on the surface of 4*PFA$_1$/PA$_{1.5}$, compared to the 4*PFA$_0$/PA$_{1.5}$ and 4*PFA$_2$/
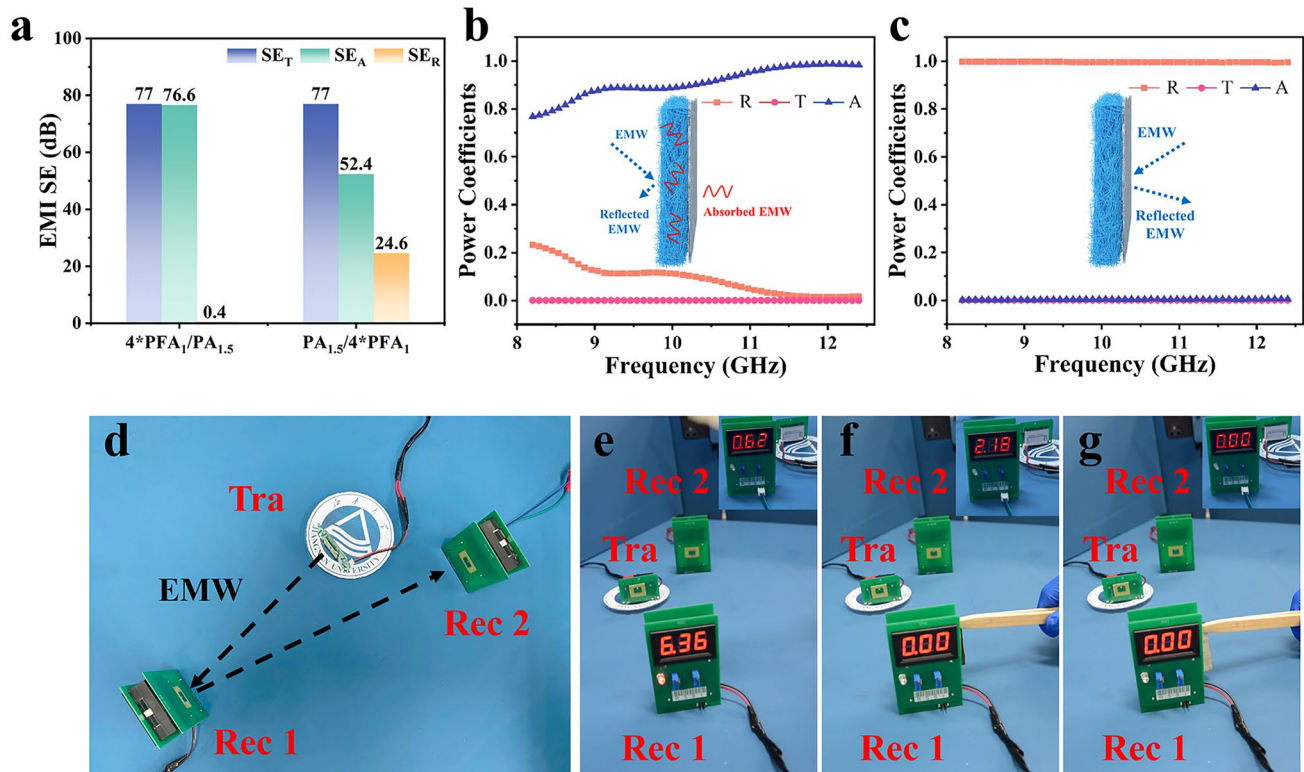

Fig. 4 **a** EMI SE of 4*PFA$_1$/PA$_{1.5}$ and PA$_{1.5}$/4*PFA$_1$. Power coefficients of **b** 4*PFA$_1$/PA$_{1.5}$ and **c** PA$_{1.5}$/4*PFA$_1$. **d** Demonstration of EMI shielding system; the changes of EMI shielding system inserted with **e** nothing, **f** PA$_{1.5}$/4*PFA$_1$, and **g** 4*PFA$_1$/PA$_{1.5}$

$PA_{1.5}$. Also, it implies that the $4*PFA_1/PA_{1.5}$ possesses an excellent impedance matching performance. Based on the above, it once again confirms the effectiveness of impedance matching structure on electromagnetic dissipation performance, inducing more EMW to enter the composite and be dissipated as much as possible. Additionally, EMI shielding performance of PA_y is analyzed by changing the plating times. As displayed in Fig. S11, the corresponding EMI SE of PA_y presents a progressive tendency to increase from 53.1 (1 h) to 67.5 dB (1.5 h), and then to 77.1 dB (2 h). Furthermore, PA_y is test by assembling an impedance matching structure ($4*PFA_1/PA_y$) with $4*PFA_1$. As shown in Fig. S13a, the corresponding EMI SE of $4*PFA_1/PA_y$ exhibits a gradual tendency to increase from 61.3 to 79.1 dB. However, the corresponding A coefficient of $4*PFA_1/PA_y$ demonstrates a minor difference, which firstly increases and then deceases (Fig. S13b). It once again confirms the effectiveness and difference of impedance matching structure on low-reflectivity EMI shielding performance.

In order to further clarify the contribution of the impedance matching structure, EMI shielding performances are investigated by controlling the incident direction of EMW. As revealed in Figs. 4a and S14a, SE_T exhibits a similar value of 77 dB, when the incident direction of EMW is set from $4*PFA_1$ to $PA_{1.5}$ ($4*PFA_1/PA_{1.5}$) or from $PA_{1.5}$ to $4*PFA_1$ ($PA_{1.5}/4*PFA_1$). However, a distinct difference arises in SE_R and SE_A. As shown in Fig. 4a and Fig. S14b, c, $4*PFA_1/PA_{1.5}$ exhibits high SE_A (~76.7 dB) and low SE_R (~0.4 dB). Conversely, $PA_{1.5}/4*PFA_1$ demonstrates lower SE_A (~52.4 dB) and higher SE_R (~24.6 dB). Accordingly, the power coefficient of $4*PFA_1/PA_{1.5}$ and $PA_{1.5}/4*PFA_1$ can be also calculated to explain the difference in EMI shielding mechanisms. As shown in Fig. 4b, c, the ultralow R coefficient (< 0.09) for $4*PFA_1/PA_{1.5}$ contrasts sharply with the ultrahigh R coefficient (~ 1) for $PA_{1.5}/4*PFA_1$. It once again confirms the effectiveness of impedance matching structure on low-reflectivity EMI shielding performance.

To clearly illustrate the different EMI shielding performances of $4*PFA_1/PA_{1.5}$ and $PA_{1.5}/4*PFA_1$, a transmitter (Tra) and two receivers (Rec 1 and Rec 2) capable of transmitting 1.0 W EMW at 10.5 GHz by antenna are fabricated as demonstrated in Fig. 4d. The number displayed on the receiver is proportional to the power of received EMW. More importantly, after being received by Rec 1, some EMW are reflected on the surface of Rec 1, and will be received by Rec 2. As a result, Rec 1 and Rec 2 exhibit the different numbers on the digital display. As shown in Fig. 4e, when the receiver accepts the wireless signal without any interference, Rec 1 shows the higher number (6.36), due to its directly received EMW generated from Tra. Meanwhile, a part of received EMW is reflected on the surface of Rec 1, due to the existence of metal components within Rec 1. As a result, Rec 2 receives a few of EMW from Rec 1, and exhibits smaller numbers (0.62). Based on the above configurations, $PA_{1.5}/4*PFA_1$ is inserted between Rec 1 and Rec 2. Moreover, $4*PFA_1$ faces to Rec 1, while $PA_{1.5}$ faces to Rec 2. The number of Rec 1 and Rec 2 rapidly turn to 0 and 2.18 (Fig. 4f and Movie S1), respectively. In contrast, the number of Rec 1 and Rec 2 sharply undergoes zero when $4*PFA_1/PA_{1.5}$ is inserted between Rec 1 and Rec 2 (Fig. 4g and Movie S2). It once again indicates that $4*PFA_1/PA_{1.5}$ nonwoven fabric effectively inhibits the reflectivity of EMW and possesses high EMI shielding performance.

3.3 Infrared Stealth Performance of Composite Nonwoven Fabrics

Thermal radiation continuously produces for all objects with temperature above absolute zero. Especially, high-temperature thermal radiation generated from equipment operation can cause significant radiation, which can be easily detected by infrared detector. Therefore, high-performance infrared stealth materials should be designed and fabricated by inhibiting those infrared radiations of objects. To characterize the infrared stealth performance of those nonwoven fabrics, the IR reflectivity in mid-infrared wavelengths is measured by FTIR spectrometer using an integrating sphere. From Fig. S15, IR reflectivity of PA_x exhibits a tendency to increase from ~ 40% to ~ 60%, and then decrease to 55% with the prolonging Ag plating time from 1 to 1.5 and 2 h. It can be attributed to the changing Ag content and roughness on the surface of PA_x fiber. Fewer Ag nanoparticles plated at a short time of 1h cannot completely cover the surface of PI fibers. Those exposed area of PI uncovered by Ag nanoparticles exhibits a low IR reflectivity characteristic, thereby endowing PA_1 with a lower IR reflectivity. Furthermore, excessed Ag nanoparticles plated at a long time of 2 h leads to the generation of aggregation on the surface of PI fibers, and an increase in roughness. It induces the formation of scattered reflection of IR wave, resulting in a decrease in IR reflectivity for PA_2.

According to Eq. 9, the corresponding IR emissivity of PA_x can be calculated and recorded in Fig. 5a. The obtained IR emissivity shows an opposite tendency with IR reflectivity. Very importantly, $PA_{1.5}$ possesses the lowest IR emissivity of 0.36 and 0.43 within 3–5 and 8–14 µm, respectively. Additionally, the formation of fluffy 3D space structure between fibers endows $4*PFA_1$ with an excellent thermal insulation capability. To observe the infrared stealth performance, $4*PFA_1/PA_{1.5}$ is placed on a thermal stage with different temperature (50–250 °C) and tested by infrared thermographer (FLUKE Ti400+). As shown in Figs. S16 and 5b, $4*PFA_1/PA_{1.5}$ displays an outstanding infrared stealth performance. The area covered by $4*PFA_1/PA_{1.5}$ can be well hidden in infrared image, which is close to deep-blue color of the background. It is worth noting that

the corresponding infrared stealth performance can be maintained at the thermal stage with a higher temperature of 250 °C. It indicates that $4*PFA_1/PA_{1.5}$ can be employed to inhibit the thermal radiation derived from high-temperature source. To further analyze the infrared stealth performance, the surface and radiation temperature of the samples are measured and recorded on a 150 °C thermal stage. As shown in Fig. 5c, the surface temperature of $4*PFA_1/PA_{1.5}$ measured by a thermocouple reaches 81.2 °C after 500 s. The difference in temperature between the surface of sample and thermal stage can be up to 62.8 °C. It can be attributed to the excellent thermal insulation capacity of nonwoven fabric. As a consequence, a lower radiation temperature of 60 °C can be easily observed by infrared thermographer after 500 s. Such outstanding high-temperature resistant
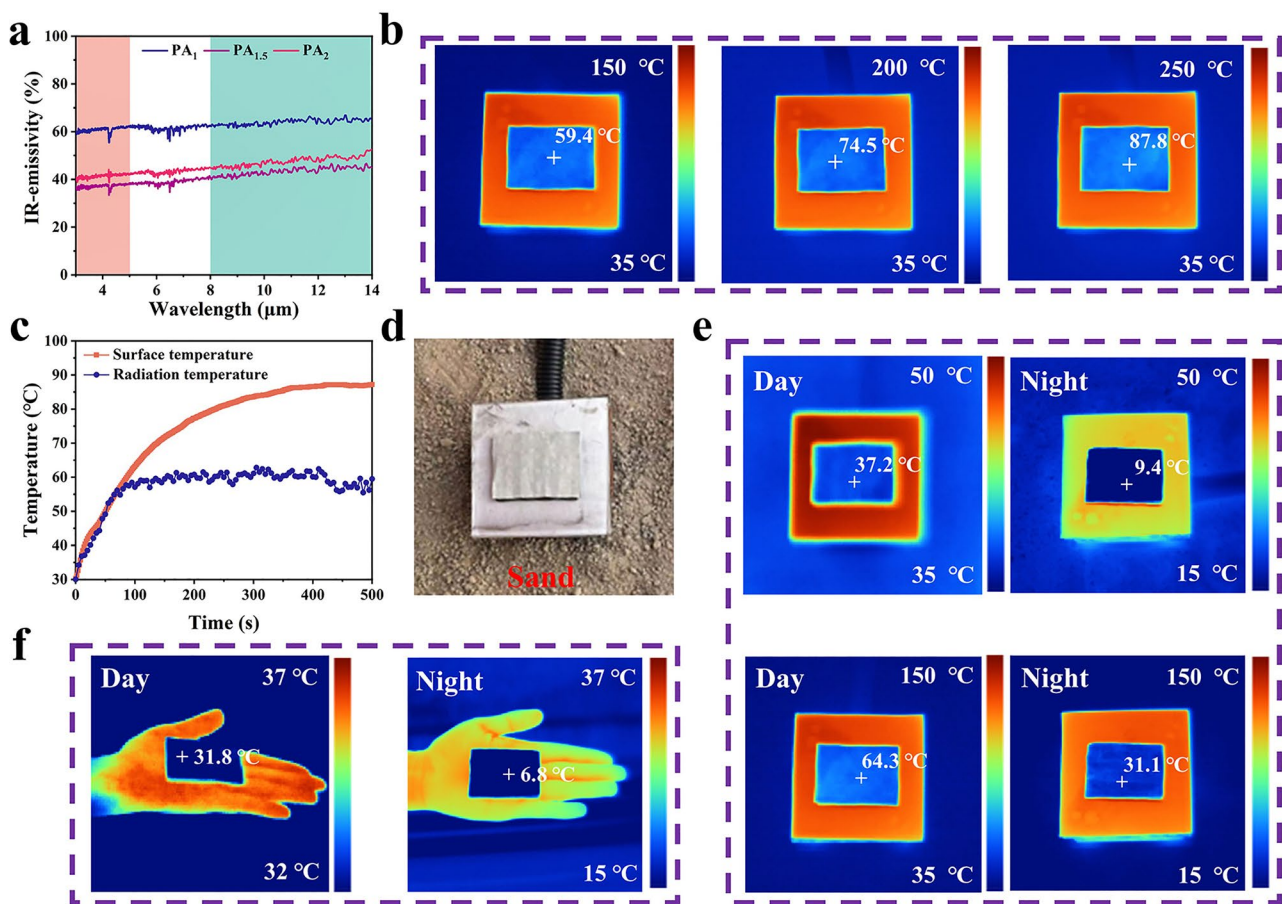

Fig. 5 **a** IR emissivity curves of PA_x. **b** IR images of $4*PFA_1/PA_{1.5}$ on the thermal stages of 150, 200, and 250 °C. **c** Surface and radiation temperature curves of $4*PFA_1/PA_{1.5}$ on the thermal stages of 150 °C. **d** Schematic diagram under simulated desert environment. **e** IR images of $4*PFA_1/PA_{1.5}$ in the simulated desert environment under different thermal stage temperatures. **f** IR images of $4*PFA_1/PA_{1.5}$ on palm

infrared stealth performance can be due to the synergistic effect of lowest IR emissivity and thermal insulation of $4*PFA_1/PA_{1.5}$. The prominent high-temperature resistant characteristic can be ascribed to the strong bonding force originated from in-situ growth of magnetic particles and "self-activated" electroless Ag plating process.

Notably, the application scenarios of infrared stealth materials may be transformed in practice, such as day and night. Very importantly, the infrared radiation of high-temperature thermal source and background in different scenarios present large differences. Therefore, infrared stealth materials are required to possess better environmental compatibility to adapt to changes in the background. Specifically, the large day/night temperature differences in desert environments are highly probable to contribute to infrared exposure. Accordingly, $4*PFA_1/PA_{1.5}$ is also placed in a simulated desert environment to monitor the infrared stealth performance during day and night. As demonstrated in Fig. 5e, excellent infrared stealth performance can be readily achieved for different thermal sources (50 and 150 °C) at day and/or night. In addition, $4*PFA_1/PA_{1.5}$ exhibits an excellent thermal camouflage for the human body (palm) as shown in Fig. 5f. During the day and night, $4*PFA_1/PA_{1.5}$ displays a darker blue color and lower temperature compared to its surroundings.

3.4 Compatible EMI Shielding/Infrared Stealth Performance of Composite Nonwoven Fabrics

With the iterative upgrading of communications technologies, the working frequency of electrical equipment gradually shifts to the higher frequency range. As shown in Fig. 6a, the EMI SE of $4*PFA_1/PA_{1.5}$ is higher than 76 dB in the typical frequency range including X-band (8.2–12.4 GHz), Ku-band (12.4–18 GHz), K-band (18–26.5 GHz), and Ka-band (26.5–40 GHz). It further verifies the excellent broadband EMI shielding performance and application potential of $4*PFA_1/PA_{1.5}$. More importantly, the rational construction of impedance matching in $4*PFA_1/PA_{1.5}$ endows it with an ultrahigh A (> 0.76) and ultralow R (< 0.24) in 8.2–40 GHz (Fig. 6b). Meantime, as shown in Fig. 6c, $4*PFA_1/PA_{1.5}$ nonwoven fabric exhibits a broadband microwave absorption performance (< -10 dB) in the range of 10.3–12.4 GHz and 13.2–35.7 GHz. It suggests that more than 90% of incident EMW are absorbed, and less than 10% of incident EMW are

reflected. It indicates that the composite possesses an excellent microwave absorption performance. Such result can be once again ascribed to the synergistic effect of impedance matching and various attenuation characteristic of $4*PFA_1/PA_{1.5}$, such as multiple scanting, conductive loss, dielectric loss, and magnetic loss (Fig. 6d). As a comparison, recently reported low-reflectivity EMI shielding materials and their performance are listed in Table S1 [30, 50–58]. As summarized in Table S1, $4*PFA_1/PA_{1.5}$ presents a significant advantage over other materials. For the compact film, an outstanding EMI SE can be easily achieved at a small thickness, whereas their high electrical conductivity severely hinders the entrance of incident EMW. For example, Guo et al. successfully fabricates an alternating multilayered film containing a $CoFe_2O_4$@MXene/cellulose nanofiber (CNF) layers and silver nanowires (AgNWs)/CNF layers [58]. A higher EMI SE performance of 87.8 dB can be reached at a low thickness of 0.1 mm. However, its high electrical conductivity (793.4 S cm^{-1}) results in a high R coefficient of 0.72. As to the foam or aerogel, low-reflectivity EMI shielding performance can be easily achieved, but a larger thickness is necessary. For instance, He et al. prepares silica/carbon nanotubes/polyimide-silver nanowires/cellulose nanofibers based on the principle of split-conductive module design [57]. Under the synergistic effect of various EMI shielding mechanisms, an excellent EMI SE of 117 dB can be obtained for the foam. The corresponding R coefficient reaches a low value of 0.005 at a big thickness of 10 mm. In practice, the huge thickness significantly reduces the convenience of materials. In this work, the average EMI SE of $4*PFA_1/PA_{1.5}$ with a density of 0.17 g cm^{-3} can be up to ~ 87 dB in 8.2–40 GHz at a smaller thickness of 2.46 mm. Importantly, the corresponding R coefficient reaches a low value of 0.07. Such excellent low-reflectivity EMI shielding performance makes it possible for $4*PFA_1/PA_{1.5}$ to become an efficient EMI shielding materials with a significant competitive advantage.

To visually illustrate the compatible EMI shielding and infrared stealth performance of $4*PFA_1/PA_{1.5}$, a demonstration is presented at a frequency of 60 GHz. As demonstrated in Fig. 6e–h and Movie S3, a display is connected to the notebook by a wireless projector (Tra) and receiver (Rec) in 60 GHz. Under normal condition, the display can show the same animation with notebook in real time by the wireless Rec (Fig. 6e). Meantime, to detect the thermal radiation of Rec in real time, the infrared
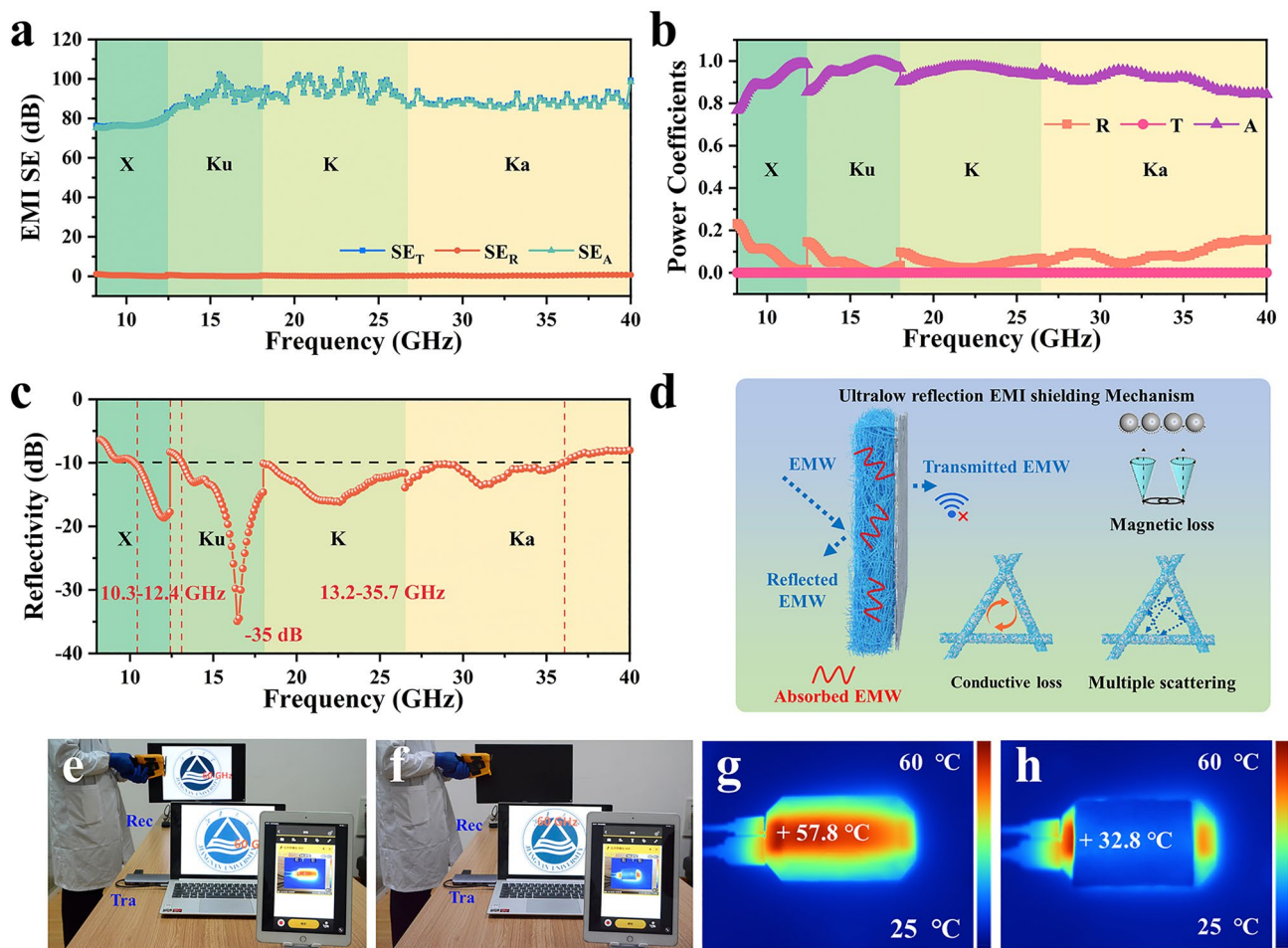
Fig. 6 **a** EMI SE, **b** power coefficients, and **c** reflectivity of 4*PFA$_1$/PA$_{1.5}$ at 8.2–40 GHz. **d** Low-reflectivity EMI shielding mechanism diagram of 4*PFA$_1$/PA$_{1.5}$. Demonstration of the compatible EMI shielding and infrared stealth performance of 4*PFA$_1$/PA$_{1.5}$ in the state of **e** original and **f** the receiver covered by 4*PFA$_1$/PA$_{1.5}$. IR images of **g** original and **h** receiver covered by 4*PFA$_1$/PA$_{1.5}$

thermographer is also connected to iPad by WiFi. Normally, the strong thermal radiation of Rec can be easily detected by infrared thermographer as shown in Fig. 6g. However, when 4*PFA$_1$/PA$_{1.5}$ covers Rec, the animation of display immediately stop (Fig. 6f). Moreover, those strong thermal radiation of Rec can be instantly inhibited (Fig. 6h). Subsequently, as 4*PFA$_1$/PA$_{1.5}$ is removed from Rec, the animation recovers at once, while the corresponding strong thermal radiation arises again. Based on the above, it can be clearly concluded that 4*PFA$_1$/PA$_{1.5}$ possesses an excellent compatible EMI shielding and infrared stealth performance. As a consequence, excellent low-reflectivity EMI shielding performance and infrared stealth performance make it promising for 4*PFA$_1$/PA$_{1.5}$ applied in military tents (Fig. 7). In detail,

the EMW emitted by the electrical equipment in military tents generates low electromagnetic reflection and high electromagnetic absorption on nonwoven fabric. It can effectively avoid EMW leakage from military tents and reduce potential secondary pollution/interference to electronic equipment and human in military tents. Importantly, electromagnetic interference from enemy can be also shielding by 4*PFA$_1$/PA$_{1.5}$ nonwoven fabric. In addition, the thermal conductivity and infrared emissivity of 4*PFA$_1$/PA$_{1.5}$ nonwoven fabric are low, thereby endowing the military tents with an excellent infrared stealth performance. In particular, the cold environment increases the possibility of infrared exposure of military equipment/humans. Excellent infrared stealth performance of 4*PFA$_1$/PA$_{1.5}$ can effectively reduce infrared radiation,

achieving infrared stealth for military equipment/humans in cold environment.

4 Conclusions

In summary, a hierarchical polyimide-based nonwoven fabric for ultralow-reflectivity EMI shielding/high-temperature resistant infrared stealth is successfully prepared by alkali treatment, in-situ growth of magnetic particles and "self-activated" electroless Ag plating process. Originated from the hydrolyzation of imide rings in PI molecules, the carboxylic active sites can be served as strong bonding anchors for Ag nanoparticles generated by Ag^+ exchange and chemical reduction, thereby facilitating the formation of "self-activated" Ag-coated PI nonwoven fabric (PA). Additionally, those carboxylic active sites provide strong adhesion for in-situ growth of Fe_3O_4 nanoparticles through complexation with Fe^{3+} and annealing treatment. Meanwhile, DA can be employed to polymerize and increase the quantity of active sites on the surface of Fe_3O_4-loaded PI nonwoven fabric. Those residual catechol and amine functional groups in PDA

effectively promote the in-situ reduction of Ag^+ to Ag nanoparticle, accelerating the "self-activated" electroless silver plating process. As a result, the impedance characteristic of Fe_3O_4/Ag-loaded PI nonwoven fabrics (PFA) can be easily adjusted. The synergistic fabrication of PFA and PA promotes the rational construction of hierarchical impedance matching in PFA/PA. It induces more EMW to enter the composite and be dissipated as much as possible, endowing it with an ultralow-reflectivity EMI shielding performance ($SE_T = 77$ dB, $R = 0.09$). Moreover, the thermal insulation of fluffy 3D space structure in PFA and IR emissivity of PA originated from Ag plating bring an excellent infrared stealth performance. More importantly, the strong adhesion interaction between Fe_3O_4, Ag, and PI fiber allows it resist the thermal stress derived from high-temperature source (250 °C), enhancing the thermal stability in EMI shielding and high-temperature resistant infrared stealth performance. Such excellent compatible ultralow-reflectivity EMI shielding/high-temperature resistant infrared stealth performance makes it possible for PFA/PA to be applied in military tent and/or camouflage.
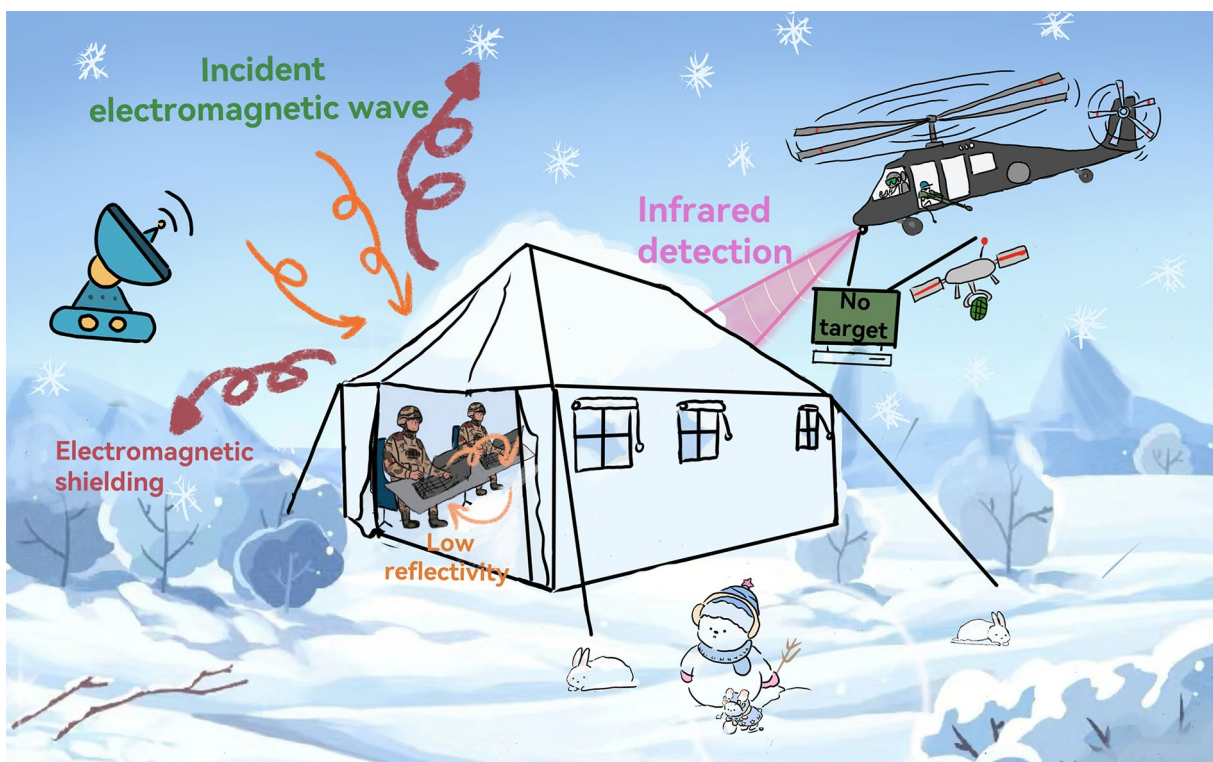

Fig. 7 The possible application scenario of 4*PFA$_1$/PA$_{1.5}$ with compatible low-reflectivity EMI shielding and infrared stealth performance

Author's Contribution Xinwei Tang contributed investigation, methodology, conceptualization, writing—original draft, and writing—review & editing. Yezi Lu and Shuangshuang Li presented methodology and supervision. Mingyang Zhu and Zixuan Wang performed validation and methodology. Yan Li, Zaiyan Hu, and Penglun Zheng carried out analysis. Zicheng Wang approved funding acquisition, investigation, methodology, conceptualization, writing—original draft, and writing—review & editing. Tianxi Liu conducted supervision, review, and funding acquisition.

Declarations

Conflict of Interests The authors declare no conflict of interest. They have no known competing financial interests or personal relationships that could have appeared to influence the work reported in this paper.

Supplementary Information The online version contains supplementary material available at https://doi.org/10.1007/s40820-024-01590-3.

References

1. H. Wei, S. Yang, P. Feng, J. Xue, F. Zhao et al., Construction of $Si_3N_4/SiO_2/SiC–Y_2Si_2O_7$ composite ceramics with gradual impedance matching structure for high-temperature electromagnetic wave absorption. Ceram. Int. **48**, 23172–23181 (2022). https://doi.org/10.1016/j.ceramint.2022.04.298

2. Z. Ma, R. Jiang, J. Jing, S. Kang, L. Ma et al., Lightweight dual-functional segregated nanocomposite foams for integrated infrared stealth and absorption-dominant electromagnetic interference shielding. Nano-Micro Lett. **16**, 223 (2024). https://doi.org/10.1007/s40820-024-01450-0

3. Y. Zhang, G. Shen, S.S. Lam, S. Ansar, S.-C. Jung et al., A waste textiles-based multilayer composite fabric with superior electromagnetic shielding, infrared stealth and flame retardance for military applications. Chem. Eng. J. **471**, 144679 (2023). https://doi.org/10.1016/j.cej.2023.144679

4. B. Yan, X. Bao, Y. Gao, M. Zhou, Y. Yu et al., Antioxidative MXene@GA-decorated textile assisted by metal ion for efficient electromagnetic interference shielding, dual-driven heating, and infrared thermal camouflage. Adv. Fiber Mater. **5**, 2080–2098 (2023). https://doi.org/10.1007/s42765-023-00330-3

5. J. Jing, H. Liu, X. Wang, Long-term infrared stealth by sandwich-like phase-change composites at elevated temperatures *via* synergistic emissivity and thermal regulation. Adv. Funct. Mater. **34**, 2309269 (2024). https://doi.org/10.1002/adfm.202309269

6. Y. Zhang, J. Gu, A perspective for developing polymer-based electromagnetic interference shielding composites. Nano-Micro Lett. **14**, 89 (2022). https://doi.org/10.1007/s40820-022-00843-3

7. M. He, J. Hu, H. Yan, X. Zhong, Y. Zhang et al., Shape anisotropic chain-like CoNi/polydimethylsiloxane composite films with excellent low-frequency microwave absorption and high thermal conductivity. Adv. Funct. Mater. (2024). https://doi.org/10.1002/adfm.202316691

8. K. Gong, Y. Peng, A. Liu, S. Qi, H. Qiu, Ultrathin carbon layer coated MXene/PBO nanofiber films for excellent electromagnetic interference shielding and thermal stability. Compos. Part A Appl. Sci. Manuf. **176**, 107857 (2024). https://doi.org/10.1016/j.compositesa.2023.107857

9. C. Liang, Z. Gu, Y. Zhang, Z. Ma, H. Qiu et al., Structural design strategies of polymer matrix composites for electromagnetic interference shielding: a review. Nano-Micro Lett. **13**, 181 (2021). https://doi.org/10.1007/s40820-021-00707-2

10. C. Liu, J. Lyu, N. Shi, Q. Cheng, Z. Liu et al., Kevlar nanofibrous aerogel-based 3-layer tandem cloak enables highly efficient and long-lasting infrared stealth. Chem. Eng. J. **462**, 142249 (2023). https://doi.org/10.1016/j.cej.2023.142249

11. M. Chen, X. Jiang, J. Huang, J. Yang, J. Wu et al., Flexible wearable $Ti_3C_2T_x$ composite carbon fabric textile with infrared stealth and electromagnetic interference shielding effect. Adv. Optical Mater. **12**, 2301694 (2024). https://doi.org/10.1002/adom.202301694

12. T. Xue, Z. Fu, D. Yu, Y. Yu, Z. Hu et al., Lightweight and flexible Ag-wrapped polyimide aerogel fabrics for electromagnetic interference shielding. Compos. Commun. **43**, 101732 (2023). https://doi.org/10.1016/j.coco.2023.101732

13. Y. Guo, K. Ruan, G. Wang, J. Gu, Advances and mechanisms in polymer composites toward thermal conduction and electromagnetic wave absorption. Sci. Bull. **68**, 1195–1212 (2023). https://doi.org/10.1016/j.scib.2023.04.036

14. X. Tang, X. Zhao, Y. Lu, S. Li, Z. Zhang et al., Flexible metalized polyimide nonwoven fabrics for efficient electromagnetic interference shielding. Chem. Eng. J. **480**, 148000 (2024). https://doi.org/10.1016/j.cej.2023.148000

15. M. Li, D. Liu, H. Cheng, L. Peng, M. Zu, Manipulating metals for adaptive thermal camouflage. Sci. Adv. **6**, eaba3494 (2020). https://doi.org/10.1126/sciadv.aba3494

16. T. Shi, D. Liu, H. Cheng, X. Wang, J. Tao, A personal thermal camouflage material based on nanofibrous polyamide membrane. Chem. Eng. J. **483**, 149342 (2024). https://doi.org/10.1016/j.cej.2024.149342

17. Z. Zeng, F. Jiang, Y. Yue, D. Han, L. Lin et al., Flexible and ultrathin waterproof cellular membranes based on high-conjunction metal-wrapped polymer nanofibers for electromagnetic interference shielding. Adv. Mater. **32**, e1908496 (2020). https://doi.org/10.1002/adma.201908496

18. F. Liu, Z. Wei, X. Hu, Y. Cai, Z. Chen et al., Asymmetric segregated network design of ultralight and thermal insulating polymer composite foams for green electromagnetic interference shielding. Compos. Commun. **38**, 101492 (2023). https://doi.org/10.1016/j.coco.2022.101492

19. M. Ma, W. Tao, X. Liao, S. Chen, Y. Shi et al., Cellulose nanofiber/MXene/FeCo composites with gradient structure for highly absorbed electromagnetic interference shielding. Chem. Eng. J. **452**, 139471 (2023). https://doi.org/10.1016/j.cej.2022.139471

20. C.J. Prabagar, S. Anand, M.C. Vu, M.-S. Tran, D. Mani et al., Thermally insulating carbon nanotubes and copper ferrite based porous polydimethylsiloxane foams for absorption-dominant electromagnetic interference shielding performance. Compos. Commun. **42**, 101691 (2023). https://doi.org/10.1016/j.coco.2023.101691

21. H. Lee, S.H. Ryu, S.J. Kwon, J.R. Choi, S.B. Lee et al., Absorption-dominant mmWave EMI shielding films with ultralow reflection using ferromagnetic resonance frequency tunable M-type ferrites. Nano-Micro Lett. **15**, 76 (2023). https://doi.org/10.1007/s40820-023-01058-w

22. C. Wu, J. Wang, X. Zhang, L. Kang, X. Cao et al., Hollow gradient-structured iron-anchored carbon nanospheres for enhanced electromagnetic wave absorption. Nano-Micro Lett. **15**, 7 (2022). https://doi.org/10.1007/s40820-022-00963-w

23. J. Hu, Y. Hu, Y. Ye, R. Shen, Unique applications of carbon materials in infrared stealth: a review. Chem. Eng. J. **452**, 139147 (2023). https://doi.org/10.1016/j.cej.2022.139147

24. R. Hu, W. Xi, Y. Liu, K. Tang, J. Song et al., Thermal camouflaging metamaterials. Mater. Today **45**, 120–141 (2021). https://doi.org/10.1016/j.mattod.2020.11.013

25. X. Fan, S. Li, W. Zhang, W. Xu, Recent progress in two-dimensional nanomaterials of graphene and MXenes for thermal camouflage. Ceram. Int. **49**, 5559–5572 (2023). https://doi.org/10.1016/j.ceramint.2022.12.034

26. Z. Deng, P. Jiang, Z. Wang, L. Xu, Z.-Z. Yu et al., Scalable production of catecholamine-densified MXene coatings for electromagnetic shielding and infrared stealth. Small **19**, e2304278 (2023). https://doi.org/10.1002/smll.202304278

27. S. Wang, R. Ding, G. Liang, W. Zhang, F. Yang et al., Direct synthesis of polyimide curly nanofibrous aerogels for high-performance thermal insulation under extreme temperature. Adv. Mater. **36**, e2313444 (2024). https://doi.org/10.1002/adma.202313444

28. W. Gu, S.J.H. Ong, Y. Shen, W. Guo, Y. Fang et al., A lightweight, elastic, and thermally insulating stealth foam with high infrared-radar compatibility. Adv. Sci. **9**, e2204165 (2022). https://doi.org/10.1002/advs.202204165

29. Y. Li, Y. Li, L. Zhao, S. Chen, S. Guo et al., Recent progress in the antidegradation strategies of two-dimensional transition metal carbides (MXenes). J. Environ. Chem. Eng. **12**, 112762 (2024). https://doi.org/10.1016/j.jece.2024.112762

30. H. Zhao, Y. Huang, Y. Han, J. Yun, X. Wang et al., Flexible and lightweight porous polyether sulfone/Cu composite film with bidirectional differential structure for electromagnetic interference shielding and heat conduction. Chem. Eng. J. **440**, 135919 (2022). https://doi.org/10.1016/j.cej.2022.135919

31. X. Zhao, X. Tang, Y. Qiao, S. Li, Z. Zhang et al., Ultrathin polyimide-based composites with efficient low-reflectivity electromagnetic shielding and infrared stealth performance. Nano Res. **17**, 6700–6712 (2024). https://doi.org/10.1007/s12274-024-6650-1

32. S. Yang, L. Tang, H. Wei, J. Xue, Z. Wang et al., *In-situ* construction of volcanic rock-like structures in Yb_2O_3 modified reduced graphene oxide and their boosted electromagnetic wave absorbing properties. Carbon **215**, 118445 (2023). https://doi.org/10.1016/j.carbon.2023.118445

33. H. Wei, Y. Yu, F. Jiang, J. Xue, F. Zhao et al., Carbon@SiC(SiCnws)-$Sc_2Si_2O_7$ ceramics with multiple loss mediums for improving electromagnetic shielding performance. J. Eur. Ceram. Soc. **42**, 2274–2281 (2022). https://doi.org/10.1016/j.jeurceramsoc.2021.12.067

34. Y. Li, K. Wu, Y. Li, S. Guo, L. Zhao et al., Recent progress in caron-based stimulus-responsive electromagnetic interference shielding materials. Nanocomposites **10**, 41–58 (2024). https://doi.org/10.1080/20550324.2023.2292878

35. M. Panahi-Sarmad, S. Samsami, A. Ghaffarkhah, S.A. Hashemi, S. Ghasemi et al., MOF-based electromagnetic shields multiscale design: nanoscale chemistry, microscale assembly, and macroscale manufacturing. Adv. Funct. Mater. **34**, 2304473 (2024). https://doi.org/10.1002/adfm.202304473

36. Z. Du, C. Zhou, H.-Y. Mi, H. Li, H. Qin et al., Recorded low-reflection in gradient MXene-decorated melamine microwave shielding foam integrated with piezoresistive sensing and energy absorption properties. Compos. Part A Appl. Sci. Manuf. **173**, 107694 (2023). https://doi.org/10.1016/j.compositesa.2023.107694

37. M. Zhou, S. Tan, J. Wang, Y. Wu, L. Liang et al., "Three-in-one" multi-scale structural design of carbon fiber-based composites for personal electromagnetic protection and thermal management. Nano-Micro Lett. **15**, 176 (2023). https://doi.org/10.1007/s40820-023-01144-z

38. A. Schander, J.M. Gancz, M. Tintelott, W. Lang, Towards long-term stable polyimide-based flexible electrical insulation for chronically implanted neural electrodes. Micromachines **12**, 1279 (2021). https://doi.org/10.3390/mi12111279

39. K. Ruan, X. Shi, Y. Zhang, Y. Guo, X. Zhong et al., Electric-field-induced alignment of functionalized carbon nanotubes inside thermally conductive liquid crystalline polyimide

composite films. Angew. Chem. Int. Ed. **62**, e202309010 (2023). https://doi.org/10.1002/anie.202309010

40. K. Ruan, J. Gu, Ordered alignment of liquid crystalline graphene fluoride for significantly enhancing thermal conductivities of liquid crystalline polyimide composite films. Macromolecules **55**, 4134–4145 (2022). https://doi.org/10.1021/acs.macromol.2c00491

41. S. Zhou, J. Dong, X. Li, X. Zhao, Q. Zhang, Continuous surface metallization of polyimide fibers for textile-substrate electromagnetic shielding applications. Adv. Fiber Mater. **5**, 1892–1904 (2023). https://doi.org/10.1007/s42765-023-00317-0

42. S. Ikeda, H. Yanagimoto, K. Akamatsu, H. Nawafune, Copper/polyimide heterojunctions: controlling interfacial structures through an additive-based, all-wet chemical process using ion-doped precursors. Adv. Funct. Mater. **17**, 889–897 (2007). https://doi.org/10.1002/adfm.200600527

43. J. Huang, D. Sun, G. Yang, H. Ma, Z. Chen et al., Facile process for surface metalization: rational design of Ag nanoparticle/polymer brush toward high-efficiency electroless plating. Compos. Sci. Technol. **231**, 109819 (2023). https://doi.org/10.1016/j.compscitech.2022.109819

44. C. Xu, P. Liu, Z. Wu, H. Zhang, R. Zhang et al., Customizing heterointerfaces in multilevel hollow architecture constructed by magnetic spindle arrays using the polymerizing-etching strategy for boosting microwave absorption. Adv. Sci. **9**, e2200804 (2022). https://doi.org/10.1002/advs.202200804

45. L. Jiao, J. Li, L.L. Richard, Q. Sun, T. Stracensky et al., Chemical vapour deposition of Fe-N-C oxygen reduction catalysts with full utilization of dense Fe-N_4 sites. Nat. Mater. **20**, 1385–1391 (2021). https://doi.org/10.1038/s41563-021-01030-2

46. Y. Cong, T. Xia, M. Zou, Z. Li, B. Peng et al., Mussel-inspired polydopamine coating as a versatile platform for synthesizing polystyrene/Ag nanocomposite particles with enhanced antibacterial activities. J. Mater. Chem. B **2**, 3450–3461 (2014). https://doi.org/10.1039/C4TB00460D

47. H. Lee, S.M. Dellatore, W.M. Miller, P.B. Messersmith, Mussel-inspired surface chemistry for multifunctional coatings. Science **318**, 426–430 (2007). https://doi.org/10.1126/science.1147241

48. S. Hong, J.S. Lee, J. Ryu, S.H. Lee, D.Y. Lee et al., Bio-inspired strategy for on-surface synthesis of silver nanoparticles for metal/organic hybrid nanomaterials and LDI-MS substrates. Nanotechnology **22**, 494020 (2011). https://doi.org/10.1088/0957-4484/22/49/494020

49. C. Zhao, Z. Yu, J. Xing, Y. Zou, H. Liu et al., Effect of Ag_2S nanocrystals/reduced graphene oxide interface on hydrogen evolution reaction. Catalysts **10**, 948 (2020). https://doi.org/10.3390/catal10090948

50. S.H. Ryu, Y.K. Han, S.J. Kwon, T. Kim, B.M. Jung et al., Absorption-dominant, low reflection EMI shielding materials with integrated metal mesh/TPU/CIP composite. Chem. Eng. J. **428**, 131167 (2022). https://doi.org/10.1016/j.cej.2021.131167

51. Z. Xie, Y. Cai, Y. Zhan, Y. Meng, Y. Li et al., Thermal insulating rubber foams embedded with segregated carbon nanotube networks for electromagnetic shielding applications. Chem. Eng. J. **435**, 135118 (2022). https://doi.org/10.1016/j.cej.2022.135118

52. B.-W. Liu, M. Cao, Y.-Y. Zhang, Y.-Z. Wang, H.-B. Zhao, Multifunctional protective aerogel with superelasticity over −196 to 500 °C. Nano Res. **15**, 7797–7805 (2022). https://doi.org/10.1007/s12274-022-4699-2

53. X. Li, M. Wu, J. Chen, X. Zhou, Q. Ren et al., A facile and large-scale approach to prepare macroscopic segregated polyether block amides/carbon nanostructures composites with a gradient structure for absorption-dominated electromagnetic shielding with ultra-low reflection. Compos. Commun. **40**, 101628 (2023). https://doi.org/10.1016/j.coco.2023.101628

54. Y. Chang, R. Hao, Y. Yang, G. Zhao, Y. Liu et al., Progressive conductivity modular assembled fiber reinforced polymer composites for absorption dominated ultraefficient electromagnetic interference shielding. Compos. Part B Eng. **260**, 110766 (2023). https://doi.org/10.1016/j.compositesb.2023.110766

55. C. Yuan, X. Li, M. Huang, F. Li, Z. Zhang et al., Multifunctional asymmetric foam with compression-enhanced EMI shielding effectiveness exhibits real-time tunability of reflection/absorption ratio and pressure sensing. Chem. Eng. J. **489**, 151359 (2024). https://doi.org/10.1016/j.cej.2024.151359

56. G.-Y. Yang, S.-Z. Wang, H.-T. Sun, X.-M. Yao, C.-B. Li et al., Ultralight, conductive $Ti_3C_2T_x$ MXene/PEDOT:PSS hybrid aerogels for electromagnetic interference shielding dominated by the absorption mechanism. ACS Appl. Mater. Interfaces **13**, 57521–57531 (2021). https://doi.org/10.1021/acsami.1c13303

57. J. He, M. Han, K. Wen, C. Liu, W. Zhang et al., Absorption-dominated electromagnetic interference shielding assembled composites based on modular design with infrared camouflage and response switching. Compos. Sci. Technol. **231**, 109799 (2023). https://doi.org/10.1016/j.compscitech.2022.109799

58. Z. Guo, P. Ren, F. Yang, T. Wu, L. Zhang et al., Robust multifunctional composite films with alternating multilayered architecture for highly efficient electromagnetic interference shielding, Joule heating and infrared stealth. Compos. Part B Eng. **263**, 110863 (2023). https://doi.org/10.1016/j.compositesb.2023.110863